ACS EARTH AND SPACE CHEMISTRY

http://pubs.acs.org/journal/aesccq

Article

Physicochemical Mixing State of Sea Spray Aerosols: Morphologies Exhibit Size Dependence

Hansol D. Lee, Samantha Wigley, Christopher Lee, Victor W. Or, Elias S. Hasenecz, Elizabeth A. Stone, Vicki H. Grassian, Kimberly A. Prather, and Alexei V. Tivanski*

Cite This: *ACS Earth Space Chem.* 2020, 4, 1604−1611

Read Online

ACCESS | Metrics & More | Article Recommendations

ABSTRACT: Sea spray aerosols (SSA) play an important role in radiative forcing by directly scattering solar radiation and indirectly by acting as cloud condensation or ice nuclei. These climate-relevant aerosol processes strongly depend on the mixing state and morphology of the individual aerosol. In this work, the distribution of different morphologies within nascent SSA as a function of particle size is investigated. SSA generated from wave breaking of natural seawater were collected for offline analysis using complementary scanning electron microscopy (SEM), thermal optical analysis, and atomic force microscopy-based photothermal infrared (AFM-PTIR) spectroscopy methods. SEM data revealed six key morphologies of SSA—prism-like, core−shell, rounded, rod-inclusion, aggregate, and rod. Of these, prism-like, core−shell, and rounded morphologies accounted for more than 99% of the entire SSA population and exhibited size-dependent trends. Thermal optical analysis data revealed a significant increase in the organic mass fraction of SSA with decreasing particle size. Concurrently, the SEM data showed a significant decrease in the relative abundance of prism-like morphology and corresponding increase of rounded and core−shell morphologies. AFM-PTIR spectroscopy showed that the SSA prism-like morphology is largely inorganic in nature, whereas the shell of the core−shell and rounded morphologies are predominantly organic. The study demonstrates that, instead of a single "representative" SSA morphology, the physicochemical mixing state of SSA is dynamic with respect to particle size. This should be taken into account to accurately predict the magnitude of the radiative forcing of SSA.

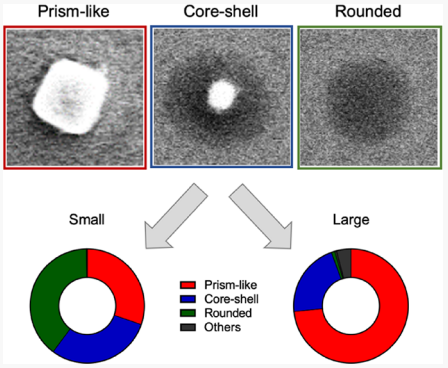

KEYWORDS: *sea spray aerosol, organic enrichment, morphology, mixing state, size, wave flume, scanning electron microscopy*

INTRODUCTION

Sea spray aerosols (SSA) affect the climate by directly scattering solar radiation and/or by seeding clouds as cloud condensation nuclei (CCN) or ice nucleating particles (INP).[1−6] Under certain circumstances, the SSA particles exhibit remarkably high selectivity—only 1 in 10^6 SSA is an effective INP at −25 °C.[6,7] These climate-relevant aerosol processes strongly depend on the physicochemical properties of the individual aerosol, such as hygroscopicity,[1,8−10] surface tension,[2,3,11−15] phase state,[16−22] and mixing state or morphology.[23−28] A population of SSA with varying morphologies yields the physicochemical mixing state of SSA.[29] Due to the abundance of both inorganic and organic species in the seawater and sea surface microlayer (SSML), SSA can exhibit core−shell morphology where the inorganic core is surrounded by the organic shell.[30] Identifying the mixing state is critical to accurately predict the aerosols' effects on the climate as the mixing state can dictate the optical properties, CCN ability, and ice nucleating potential of a variety of aerosol types.[29,31]

The physical and chemical mixing states of nascent SSA generated from wave breaking of seawater were previously reported in several wave flume studies. In 2013, Ault et al. reported sea salt-organic (SS-OC, equivalent to the core−shell morphology), organic carbon (OC), and other particle types to identify the chemical mixing state of SSA using scanning electron microscopy coupled with energy dispersive X-ray spectrometry (SEM−EDX) and transmission electron microscopy (TEM).[32] In 2017, Pham et al. reported sea salt (equivalent to the core−shell morphology), organic salt agglomerate, homogeneous organics, and needle-like particle types to identify the physical and chemical mixing states of SSA using scanning transmission X-ray microscopy (STXM).[33] Across these two studies, the number of particle morphologies

Received: June 12, 2020
Revised: July 31, 2020
Accepted: August 4, 2020
Published: August 4, 2020

observed for nascent SSA differed. The two also differed in the relative number of core−shell equivalent morphologies such as SS-OC and sea salt as a function of particle size. These results collectively raise three questions for the nascent SSA: first, is there a "representative" morphology and mixing state? Second, how many different morphologies exist? Third, is there a size dependence of these different morphologies?

Here, we report findings on the dynamic nature of the physicochemical mixing state of nascent SSA with respect to particle size. A mesocosm experiment was conducted in the summer of 2018 at Scripps Institution of Oceanography using a sealed wave flume channel, which contained seawater from the south coast of California. Nascent SSA were generated from wave breaking and collected on substrates for offline single-particle analysis using SEM, atomic force microscopy-based photothermal infrared (AFM-PTIR) spectroscopy, and bulk analysis using thermal optical analysis. Single-particle results from SEM show six unique morphological types of SSA with three (prism-like, core−shell, and rounded) representing the majority of SSA with aerodynamic diameters ranging from 0.10 to 1.8 μm. Interestingly, the relative abundance of these three main morphological types is shown to depend on the particle size. The results from the AFM-PTIR confirm that the prism-like morphology is largely inorganic, whereas the shell from core−shell and rounded morphologies are predominantly organic. These results are relevant to the atmospheric theoretical frameworks that require precise knowledge of the mixing state and/or individual particle morphology to predict the SSA's climate-related effects.

MATERIALS AND METHODS

Particle Generation for Offline Analysis. Sea spray aerosols were generated through wave breaking of California coast seawater contained in a wave flume. Experimental details of the seawater collection, storage, and operation of the wave flume are published elsewhere[34] and were replicated in this study, except for the addition of nutrients to induce a phytoplankton growth. While some modifications of the wave flume have been made since the previous study, size distribution measurements and single-particle chemical measurements of the generated SSA observed were very similar to the one observed in earlier campaigns,[34,35] demonstrating that these modifications had no significant effect on the physicochemical properties of the generated nascent SSA. A micro-orifice uniform deposit impactor (MOUDI; MSP, Inc., model 110) was used to deposit SSA particles onto hydrophobically coated silicon wafers (Ted Pella, Inc.) and cleaned aluminum foil substrates (47 mm, TSI, Inc.). The aerosol stream from the wave flume was approximately 80% relative humidity (RH). Substrate-deposited aerosol samples were stored in cleaned Petri dishes housed in a laminar flow hood (NuAire, Inc., NU-425-400) for SEM experiments and frozen (−20 °C) for thermal optical analysis and high-performance ion exchange chromatography.

Single-Particle Scanning Electron Microscopy. Field emission S-4800 SEM (Hitachi, Tokyo, Japan) was used to image individual SSA and categorize them based on the morphology. Silicon wafers with substrate-deposited particles were mounted onto aluminum stubs (Ted Pella, Inc.) to insert the samples into the vacuum chamber. An accelerating voltage of 5 keV and a working distance of 20 nm were used for imaging. The pixel size ranged from 7 to 33 nm where smaller particles were imaged with a smaller pixel size. No additional coating of the substrate-deposited particles was performed.

Single-Particle Atomic Force Microscopy-Based Photothermal Infrared Spectroscopy. AFM-PTIR measurements were conducted using a commercial nanoIR2 (Bruker, Santa Barbara, CA) microscopy system equipped with a tunable mid-IR optical parametric oscillator laser. Experiments were performed at ambient relative humidity (20−40%) and temperature (23−26 °C). Images were collected in tapping mode at a scan rate of 0.5 Hz using silicon nitride probes with a chromium-gold coating (HQ: NSC19/CR-AU, Mikro-Masch) with a tip radius of 35 nm and a nominal spring constant range of 0.05−2.3 N/m. PTIR spectra were collected at a preselected tip-localized position across the sample surface with a nominal spatial resolution of <35 nm and a spectral resolution of 8 cm^{-1} while co-averaging 128 laser pulses. To facilitate direct comparison, all PTIR spectra shown were obtained with the same laser power (idler pulse energy of 0.2 μJ at 7000 nm) using the same AFM tip. All PTIR spectra shown were taken on a single point without smoothing filters applied. To account for a possible substrate PTIR signal contribution, a spectrum was taken on the substrate and subtracted from all corresponding spectra obtained for imaged individual particles.

Organic and Inorganic Mass Fraction Measurements. Organic carbon and common cations and anions were quantified using established methods and only briefly summarized below.[36−38] For organic carbon analysis, a triangular punch corresponding to one-eighth of the filter area was subsampled and analyzed using a thermal optical analyzer (Sunset Laboratories, Forest Grove, OR) following the ACE-Asia protocol.[36] Another one-eighth of the subsample was extracted with 4 mL of ultrapure water (UP; 18.2 MΩ·cm, Thermo Barnstead EasyPure II) via 100 min of mechanical shaking and then filtered (0.45 μm polypropylene Whatman) prior to analysis. Cations (lithium, sodium, ammonium, potassium, magnesium, and calcium) and anions (fluoride, chloride, nitrate, nitrite, bromide, phosphate, and sulfate) were separated and quantified via high-performance ion exchange chromatography with conductivity detection (Dionex ICS-5000, Sunnyvale, CA).[37,38] Inorganic mass was estimated as sea salt by converting the mass of sodium measured to the mass of sea salt using the sodium/sea salt ratio previously determined from seawater salt composition.[39]

RESULTS AND DISCUSSION

Production and Collection of Sea Spray Aerosols in the Wave Flume. In 2018, wave flume experiments were carried out using an ocean−atmosphere interaction facility filled with natural seawater from the Southern California coast. This was similar to studies performed in 2014 but with the exclusion of the nutrients that would have induced a phytoplankton bloom.[30] Nascent SSA produced from wave breaking within the flume were collected for offline studies using a MOUDI at ca. 80% RH, which is greater than both the deliquescence and efflorescence relative humidity of NaCl.[10] While this may introduce varying efflorescence behaviors of the particles upon impaction and dehydration, we note that the wet deposition was shown previously to be an ideal method to minimize the morphology-deforming effects of the particle impaction.[28] All particles are assumed to have achieved thermodynamic equilibrium at this relative humidity, given that the characteristic time of bulk diffusion is less than 1 s.[40]

https://dx.doi.org/10.1021/acsearthspacechem.0c00153
ACS Earth Space Chem. 2020, 4, 1604−1611

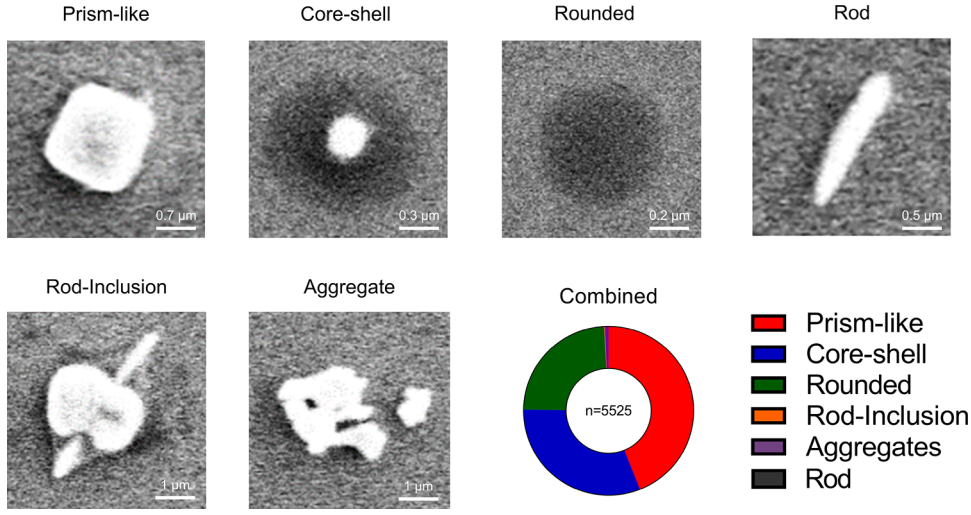

Figure 1. Selected illustrative scanning electron micrographs of six morphological categories identified for nascent sea spray aerosols. A combined total of 5525 individual particles were characterized, and the percent breakdown for each morphology is shown in the colored pie chart. Percentages are shown in Table 1.

Table 1. Summary of Morphological Categories of Nascent Sea Spray Aerosols Grouped Based on Corresponding Particle Size Ranges as Determined from the MOUDI Cutoff Size Ranges at 80% Relative Humidity

		percent distributions based on particle size at 80% relative humidity				
morphology	total 0.10−1.8 μm (%)	1.0−1.8 μm (%)	0.56−1.0 μm (%)	0.32−0.56 μm (%)	0.18−0.32 μm (%)	0.10−0.18 μm (%)
prism-like	44.0	73.5	65.9	23.4	41.2	30.3
core−shell	31.2	21.0	32.9	38.3	19.6	29.9
rounded	23.9	1.0	0.1	38.3	39.2	39.5
rod-inclusion	0.1	0.5	0.2	0.0	0.0	0.0
aggregate	0.7	4.1	0.7	0.0	0.0	0.2
rod	0.1	0.0	0.1	0.1	0.0	0.1

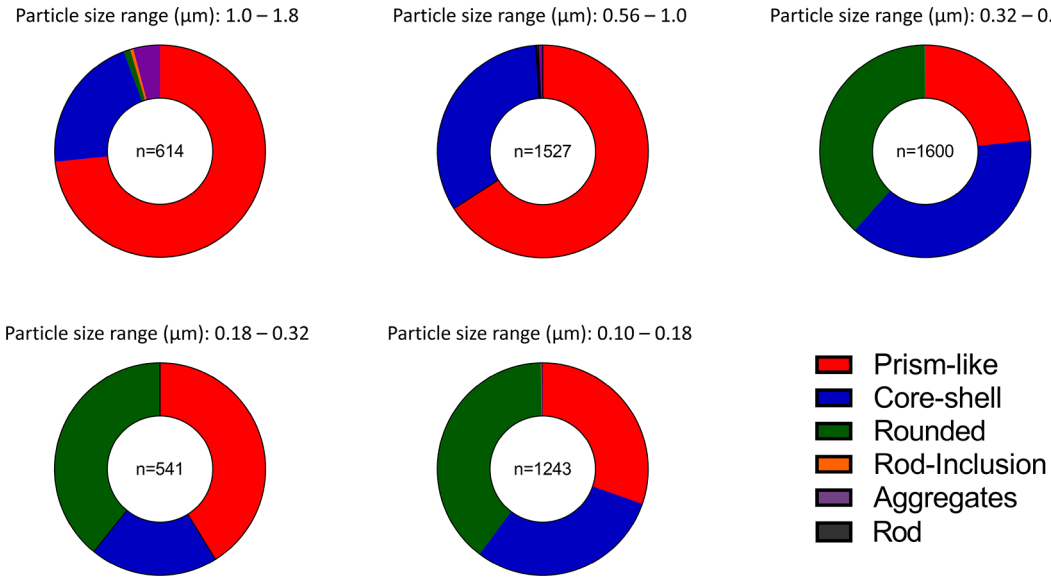

Figure 2. Distribution of the morphological categories based on the particle cutoff size ranges from MOUDI impactor stages 5 (largest, top left) to 9 (smallest, bottom middle) at 80% RH. Percentages are shown in Table 1.

Particles were collected within stages 9−5 of the MOUDI, which corresponds to an aerodynamic diameter size range of 0.10−1.8 μm. The particles at 80% RH are assumed to be spherical prior to impaction. These stage-specific size ranges correspond to particle sizes at ca. 80% RH, and upon drying on the substrate, the particles will become smaller.[9]

Collective and Size-Separated Morphological Analysis of Sea Spray Aerosols. Figure 1 illustrates the six unique morphological types of nascent SSA identified in this work. All data correspond to SSA collected on the same day of the wave flume experiment. Overall, a total of 5525 individual particles with an aerodynamic diameter size range of 0.10−1.8

https://dx.doi.org/10.1021/acsearthspacechem.0c00153
ACS Earth Space Chem. 2020, 4, 1604−1611

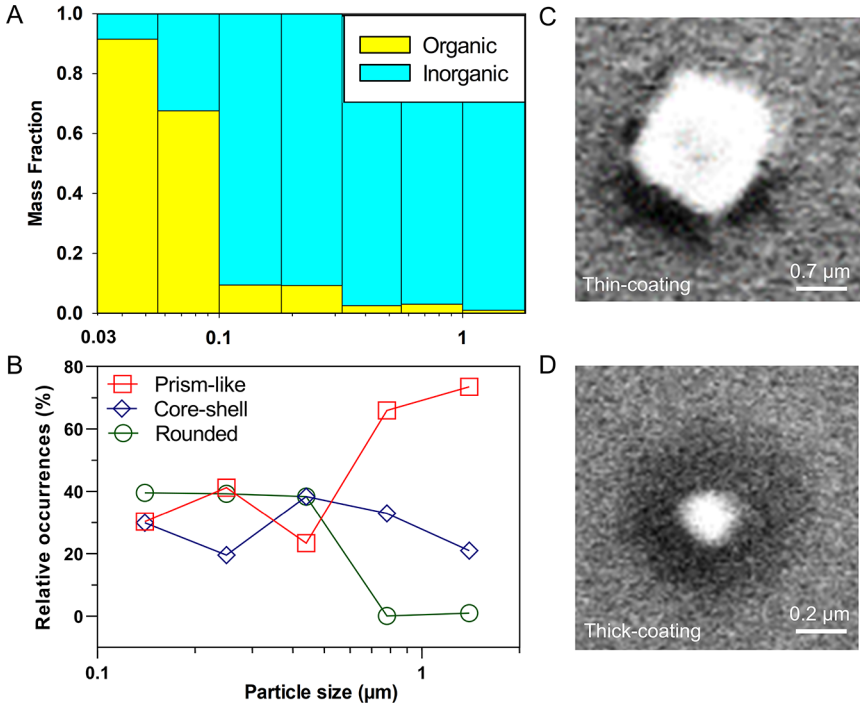

Figure 3. (A) Organic (yellow) and inorganic (cyan) mass fractions versus particle size. The width of the bars indicates the MOUDI cutoff size range at 80% RH. (B) Relative occurrences of morphological categories versus the particle size for the three most frequently observed morphologies. The average taken from the MOUDI cutoff sizes for each stage was used. Solid colored lines are shown for illustrative purposes. (C, D) Scanning electron micrographs of individual core−shell sea spray aerosols with a (C) relatively thin coating on the larger particle and a (D) relatively thick coating on the smaller particle.

μm has been assessed for the morphology using SEM. The categorization of morphology was performed qualitatively for individual SSA particles. Here, we note that any discussion *ex nunc* regarding the morphological distribution within the SSA population will be termed a "mixing state". In this work, we only refer to the physicochemical mixing state.[29] The six unique morphological types identified were prism-like, core−shell, rounded, rod, rod-inclusion, and aggregate morphologies (Figure 1). The bright versus dark contrast in the micrographs, which is in part indicative of the height or thickness of the particles, was used as one of the determinants of a morphology. Prism-like morphology showed a characteristic bright contrast in the micrographs and rectangular shape edges outlining the particle. Core−shell morphology showed prism-like particles as cores encased by a rounded shell that showed a characteristic dark contrast in the micrographs. We note that the relative abundance of core−shell morphology may be underreported in this study as particles that were characterized as having prism-like morphology may retain thin organic shells that are not readily apparent in the SEM micrographs due to inherent spatial resolution limitations. Rounded morphology showed a dark-filled circular shape, similar to the core−shell morphology but without the visible bright contrast core in the center. Rod morphology showed a bright contrast with an elongated shape indicative of a high aspect ratio (i.e., ratio of the length over diameter). Rod-inclusion morphology showed a bright contrast with a rod attached to a secondary feature. Finally, aggregate morphology showed a bright contrast with a cluster of small, irregular particles. Collectively, the prism-like morphology was the most abundant (44.0%) followed by core−shell morphology (31.2%) and rounded morphology (23.9%) (Table 1). The three combined morphologies represented 99.1% of the entire SSA population studied here. The remaining 0.9% of the SSA was from the aggregate morphology (0.7%), rod morphology (0.1%), and rod-inclusion morphology (0.1%). Next, the mixing state will be further assessed as a function of particle size.

Figure 2 shows the morphological categorization based on the particle size ranges (derived from the MOUDI stage cutoff sizes). While the collective mixing state data revealed low abundance of the aggregate, rod, and rod-inclusion morphologies, these morphologies still show distinct trends with decreasing size. The rod-inclusion and aggregate morphologies have their greatest abundance in the largest size range (1.0−1.8 μm) at 0.5 and 4.1%, respectively. Their relative abundances decrease with decreasing particle size, showing a rod-inclusion morphology at 0.2% and an aggregate morphology at 0.7% for the smaller size range (0.56−1.0 μm). While the rod-inclusion morphology is absent below 0.56 μm, the aggregate morphology is not observed as the size range decreases (0.18−0.56 μm), only to reappear at 0.2% (0.10−0.18 μm). In comparison, the rod morphology is initially absent (1.0−1.8 μm) and then present in a low but stable relative occurrence at 0.1% (0.10−0.18 and 0.32−1 μm). Next, the effect of decreasing particle size on the relative abundance of three main morphologies, prism-like, core−shell, and rounded morphologies will be discussed in the context of concurrent size-dependent changes in the chemical composition of SSA.

The Effect of Composition and Size on Sea Spray Aerosol Mixing State. To understand the relationship between the composition and the mixing state of the SSA, the bulk organic carbon relative to sea salt ratios were measured using thermal optical analysis of aluminum foil substrates collected at different MOUDI stages. Thermal optical analysis is a reliable technique that has been applied to aerosols previously.[37] The substrates were used to collect the

https://dx.doi.org/10.1021/acsearthspacechem.0c00153
ACS Earth Space Chem. 2020, 4, 1604−1611

SSA concurrently with the silicon wafer SEM substrates studied above. Figure 3A shows the organic and inorganic mass fractions measured as a function of size from 0.03 to 1.8 μm in particle size. The same MOUDI cutoff sizes for the single-particle analysis were also used here. *Ex nunc*, the average of the particle size range taken from the MOUDI cutoff sizes will be used to discuss the data. With decreasing size, a gradual increase in the relative organic content is evident from an organic mass fraction of 0.010 ± 0.002 (1.4 μm) to 0.030 ± 0.003 (0.78 μm) followed by a small decrease to 0.026 ± 0.006 (0.44 μm) and a subsequent increase to 0.09 ± 0.02 (0.25 μm) and 0.09 ± 0.02 (0.14 μm). Then, there is a large increase to 0.7 ± 0.2 (0.078 μm) and finally again to 0.91 ± 0.07 (<0.078 μm). An increasing organic content of nascent SSA was observed with decreasing particle sizes, which may give rise to a discernible change in the particle morphology. Thus, assuming that the prism-like morphology is predominantly inorganic and rounded morphology is predominantly organic, the following hypothesis can be formulated: the relative abundances of different morphologies will correlate with the increasing organic content as the particle size decreases. Furthermore, the relative organic coating thickness of core−shell SSA may also increase as the particle size decreases since the shell portion of the core−shell may be predominantly organic in composition.

To test the hypothesis, the relationship between the particle size and morphology was investigated (Figure 3B). The data displays the size-dependent relative occurrences of prism-like, core−shell, and rounded morphologies. As before, the discussion revolves around the average particle size calculated from the MOUDI cutoff size range. The prism-like morphology is most abundant at 73.5% (1.4 μm) followed by a small decrease to 65.9% (0.78 μm). Then, there was a precipitous decrease to 23.4% (0.44 μm) followed by an increase to 41.2% (0.25 μm) before decreasing to 30.3% (0.14 μm). The rounded morphology showed an opposite trend with respect to the decrease in particle size where it was initially least abundant at 1.0% (1.4 μm) and showed a small decrease to 0.1% (0.78 μm) before drastically increasing to 38.3% (0.44 μm). With a further decrease in size, the relative abundance is stable at 39.2 (0.25 μm) and 39.5% (0.14 μm). Unlike the prism-like and rounded morphologies, the core−shell morphology showed a moderate increase in abundance from 21 (1.4 μm) to 32.9 (0.78 μm) and 38.3% (0.44 μm) before decreasing to 19.6% (0.25 μm). Below this size, there is an increase to 29.9% (0.14 μm). Taken together, the data reveals that an increase in organic mass fraction with a decrease in size leads to a decrease in the relative abundance of prism-like particles and an increase in the relative abundance of rounded morphologies. These results agree with previous findings.[32] Also, the core−shell SSA display variable shell thicknesses as a function of size. Specifically, the larger core−shell particles generally exhibited relatively thinner coatings (Figure 3C), whereas the smaller core−shell particles exhibited thicker coatings relative to the smaller particle size (Figure 3D).

Figure 4 shows tip localized AFM-PTIR spectra taken across six selected representative individual particles that correspond to the three major morphological categories observed in this work—prism-like, core−shell, and rounded. In the spectral range examined, peaks that can be indicative of organics appear in the spectra at the 1300−1450 cm^{-1} range corresponding to δ (CH_2, CH_3) modes.[41−44] These peaks are most prevalent in spectra corresponding to the rounded organic particle (cyan)

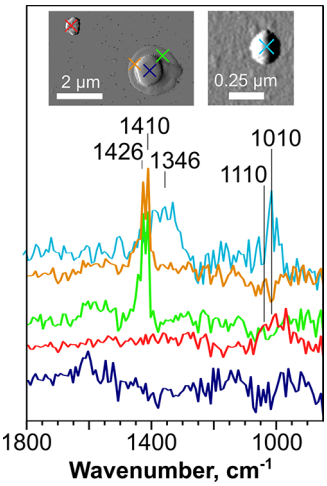

Figure 4. Substrate-subtracted AFM-PTIR spectra of particles with three main nascent SSA morphologies: prism-like (red), rounded (cyan), and core−shell (blue, core; orange and green, shell). Insets show AFM amplitude images with corresponding colored markers where the spectra were collected.

and the thin shell of the core−shell particle (orange and green). In contrast, the low IR activity of the corresponding core suggests an IR inactive salt core (likely NaCl), while the prism-like particle shown has a small peak at around 1110 cm^{-1}, which can be assigned to stretching modes of sulfates or silicates.[45,46] Spectral intensities are expected to scale with increasing particle thickness and viscosity.[41,47] However, the most intense IR active regions of the particles shown are in the thin core−shell coating and the small rounded organic particle, suggesting that the particle shell and the small rounded particle are relatively rich in organic compounds. While the thin organic shell is IR-active around the δ (CH_2, CH_3) modes, the larger particle core is expected to contribute more to the overall particle mass. In contrast, the smaller rounded particle is organic-rich, and the spectra of these thin particles suggest that the organic fraction is relatively high. These results are consistent with the bulk organic mass fraction measurements discussed above wherein the relative fraction of organics is enhanced in the smaller particles. Furthermore, the results confirm our previous assumption that the prism-like particles are predominantly inorganic, the core−shell particles have organic shells and an inorganic core, and the rounded particles are predominantly organic.

The data thus far reveal a dynamic mixing state with respect to particle size. The lack of a single representative morphology of nascent SSA has potential implications in the atmospheric modeling. For various aerosol types, accurately measuring the optical properties and predicting their direct aerosol effects depend strongly on accurate information on the mixing state.[48] Assuming one representative mixing state for a specific aerosol to infer its direct aerosol effect, irrespective of the size, may lead to erroneous predictions on the magnitude of the radiative forcing. In addition, the mixing state of aerosols is also important to accurately predict the CCN concentrations and hence properly evaluating the indirect effect of SSA.[29] In both cases, the mixing state or morphological distribution of nascent SSA thus should not be assumed to extrapolate accurately from one size range to the other. Instead, the dynamic and size-dependent nature of the SSA mixing state should be taken into

https://dx.doi.org/10.1021/acsearthspacechem.0c00153
ACS Earth Space Chem. 2020, 4, 1604−1611

account in future studies to accurately quantify and predict SSA's climate-related effects.

CONCLUSIONS

The physicochemical mixing state (i.e., morphological distribution) of nascent sea spray aerosols generated from wave breaking was investigated as a function of size. Thermal optical analysis revealed that the sea spray aerosols exhibited an increase in organic mass fraction with decreasing particle size. Concurrently, the single-particle scanning electron microscopy data revealed six distinct morphological types—prism-like, core−shell, rounded, rod-inclusion, aggregate, and rod. The prism-like, core−shell, and rounded morphologies constituted more than 99% of the entire population of nascent SSA studied here. As a function of size, however, the prism-like morphology was the most abundant and rounded morphology was the least abundant within the 0.56−1.8 μm size range. With decreasing particle size, the relative abundance of the prism-like morphology decreased, while that of the rounded and core−shell morphologies increased. Smaller core−shell particles exhibited a thicker relative coating thickness compared to larger core−shell particles. Finally, the data from atomic force microscopy-based photothermal infrared spectroscopy indicated that the prism-like morphology had predominantly inorganic composition, whereas the shell of the core−shell and rounded morphologies had predominantly organic composition. In summary, sea spray aerosols did not exhibit a specific representative morphology across all sizes. While some of these findings were published in other works, this work provides further evidence of the dynamic and size-dependent nature of the physicochemical mixing state of sea spray aerosols.

AUTHOR INFORMATION

Corresponding Author

Alexei V. Tivanski − *Department of Chemistry, University of Iowa, Iowa City, Iowa 52242, United States*; Email: alexei-tivanski@uiowa.edu

Authors

Hansol D. Lee − *Department of Chemistry, University of Iowa, Iowa City, Iowa 52242, United States*

Samantha Wigley − *Department of Chemistry, University of Iowa, Iowa City, Iowa 52242, United States*

Christopher Lee − *Scripps Institution of Oceanography, University of California, San Diego, La Jolla, California 92037, United States*

Victor W. Or − *Department of Chemistry and Biochemistry, University of California at San Diego, La Jolla, California 92093, United States*

Elias S. Hasenecz − *Department of Chemistry, University of Iowa, Iowa City, Iowa 52242, United States*

Elizabeth A. Stone − *Department of Chemistry, University of Iowa, Iowa City, Iowa 52242, United States*

Vicki H. Grassian − *Scripps Institution of Oceanography, University of California, San Diego, La Jolla, California 92037, United States; Department of Chemistry and Biochemistry, University of California at San Diego, La Jolla, California 92093, United States;* orcid.org/0000-0001-5052-0045

Kimberly A. Prather − *Scripps Institution of Oceanography and Department of Nanoengineering, University of California, San Diego, La Jolla, California 92037, United States; Department of Chemistry and Biochemistry, University of California at San Diego, La Jolla, California 92093, United States*

Complete contact information is available at: https://pubs.acs.org/10.1021/acsearthspacechem.0c00153

Author Contributions

The manuscript was written through contributions of all authors. All authors have given approval to the final version of the manuscript. Project administration: K.A.P., V.H.G., E.A.S., and A.V.T. Sample and data collection: H.D.L., S.W., C.L., V.W.O., and E.S.H. Writing: H.D.L., V.W.O., E.S.H., C.L., E.A.S, V.H.G., and A.V.T.

Notes

The authors declare no competing financial interest.

The data for this publication can be retrieved from the UC San Diego Library Digital Collections. https://doi.org/10.6075/J0513WQN.

ACKNOWLEDGMENTS

This work was funded by the National Science Foundation (NSF) through the NSF Center for Aerosol Impacts on Chemistry of the Environment (CAICE) under grant no. CHE-1801971. H.D.L. was partially supported by a University of Iowa Graduate College Summer Fellowship and an ACS Division of Analytical Chemistry & Eastman Chemical Company Summer Graduate Fellowship. Any opinions, findings, and conclusions or recommendations expressed in this material are those of the authors and do not necessarily reflect the views of the National Science Foundation. H.D.L. acknowledges the use of the University of Iowa Central Microscopy Research Facility, a core resource supported by the University of Iowa Vice President for Research, and the Carver College of Medicine.

REFERENCES

(1) Petters, M. D.; Kreidenweis, S. M. A single parameter representation of hygroscopic growth and cloud condensation nucleus activity. *Atmos. Chem. Phys.* **2007**, *7*, 1961−1971.

(2) Ovadnevaite, J.; Zuend, A.; Laaksonen, A.; Sanchez, K. J.; Roberts, G.; Ceburnis, D.; Decesari, S.; Rinaldi, M.; Hodas, N.; Facchini, M. C.; Seinfeld, J. H.; Dowd, C. O. Surface tension prevails over solute effect in organic-influenced cloud droplet activation. *Nature* **2017**, *546*, 637−641.

(3) Ruehl, C. R.; Davies, J. F.; Wilson, K. R. An interfacial mechanism for cloud droplet formation on organic aerosols. *Science* **2016**, *351*, 1447−1450.

(4) DeMott, P. J.; Hill, T. C. J.; Petters, M. D.; Bertram, A. K.; Tobo, Y.; Mason, R. H.; Suski, K. J.; McCluskey, C. S.; Levin, E. J. T.; Schill, G. P.; Boose, Y.; Rauker, A. M.; Miller, A. J.; Zaragoza, J.; Rocci, K.; Rothfuss, N. E.; Taylor, H. P.; Hader, J. D.; Chou, C.; Huffman, J. A.; Pöschl, U.; Prenni, A. J.; Kreidenweis, S. M. Comparative measurements of ambient atmospheric concentrations of ice nucleating particles using multiple immersion freezing methods and a continuous flow diffusion chamber. *Atmos. Chem. Phys.* **2017**, *17*, 11227−11245.

(5) McCluskey, C. S.; Hill, T. C. J.; Malfatti, F.; Sultana, C. M.; Lee, C.; Santander, M. V.; Beall, C. M.; Moore, K. A.; Cornwell, G. C.; Collins, D. B.; Prather, K. A.; Jayarathne, T.; Stone, E. A.; Azam, F.; Kreidenweis, S. M.; DeMott, P. J. A Dynamic Link between Ice Nucleating Particles Released in Nascent Sea Spray Aerosol and Oceanic Biological Activity during Two Mesocosm Experiments. *J. Atmos. Sci.* **2017**, *74*, 151−166.

(6) DeMott, P. J.; Hill, T. C. J.; McCluskey, C. S.; Prather, K. A.; Collins, D. B.; Sullivan, R. C.; Ruppel, M. J.; Mason, R. H.; Irish, V. E.; Lee, T.; Hwang, C. Y.; Rhee, T. S.; Snider, J. R.; McMeeking, G. R.; Dhaniyala, S.; Lewis, E. R.; Wentzell, J. J. B.; Abbatt, J.; Lee, C.;

Sultana, C. M.; Ault, A. P.; Axson, J. L.; Martinez, M. D.; Venero, I.; Santos-Figueroa, G.; Dale Stokes, M.; Deane, G. B.; Mayol-Bracero, O. L.; Grassian, V. H.; Bertram, T. H.; Bertram, A. K.; Moffett, B. F.; Franc, G. D. Sea spray aerosol as a unique source of ice nucleating particles. *Proc. Natl. Acad. Sci. U. S. A.* **2016**, *113*, 5797−5803.

(7) DeMott, P. J.; Prenni, A. J.; Liu, X.; Kreidenweis, S. M.; Petters, M. D.; Twohy, C. H.; Richardson, M. S.; Eidhammer, T.; Rogers, D. C. Predicting global atmospheric ice nuclei distributions and their impacts on climate. *Proc. Natl. Acad. Sci. U. S. A.* **2010**, *107*, 11217−11222.

(8) Forestieri, S. D.; Cornwell, G. C.; Helgestad, T. M.; Moore, K. A.; Lee, C.; Novak, G. A.; Sultana, C. M.; Wang, X.; Bertram, T. H.; Prather, K. A.; Cappa, C. D. Linking variations in sea spray aerosol particle hygroscopicity to composition during two microcosm experiments. *Atmos. Chem. Phys.* **2016**, *16*, 9003−9018.

(9) Morris, H. S.; Estillore, A. D.; Laskina, O.; Grassian, V. H.; Tivanski, A. V. Quantifying the Hygroscopic Growth of Individual Submicrometer Particles with Atomic Force Microscopy. *Anal. Chem.* **2016**, *88*, 3647−3654.

(10) Estillore, A. D.; Morris, H. S.; Or, V. W.; Lee, H. D.; Alves, M. R.; Marciano, M. A.; Laskina, O.; Qin, Z.; Tivanski, A. V.; Grassian, V. H. Linking hygroscopicity and the surface microstructure of model inorganic salts, simple and complex carbohydrates, and authentic sea spray aerosol particles. *Phys. Chem. Chem. Phys.* **2017**, *19*, 21101−21111.

(11) Davies, J. F.; Zuend, A.; Wilson, K. R. Technical note: The role of evolving surface tension in the formation of cloud droplets. *Atmos. Chem. Phys.* **2019**, *19*, 2933−2946.

(12) Forestieri, S. D.; Staudt, S. M.; Kuborn, T. M.; Faber, K.; Ruehl, C. R.; Bertram, T. H.; Cappa, C. D. Establishing the impact of model surfactants on cloud condensation nuclei activity of sea spray aerosol mimics. *Atmos. Chem. Phys.* **2018**, *18*, 10985−11005.

(13) Lee, H. D.; Estillore, A. D.; Morris, H. S.; Ray, K. K.; Alejandro, A.; Grassian, V. H.; Tivanski, A. V. Direct Surface Tension Measurements of Individual Sub-Micrometer Particles Using Atomic Force Microscopy. *J. Phys. Chem. A* **2017**, *121*, 8296−8305.

(14) Bzdek, B. R.; Power, R. M.; Simpson, S. H.; Reid, J. P.; Royall, C. P. Precise, contactless measurements of the surface tension of picolitre aerosol droplets. *Chem. Sci.* **2016**, *7*, 274−285.

(15) Morris, H. S.; Grassian, V. H.; Tivanski, A. V. Humidity-dependent surface tension measurements of individual inorganic and organic submicrometre liquid particles (vol 6, pg 3242, 2015). *Chem. Sci.* **2015**, *6*, 6021−6021.

(16) Tandon, A.; Rothfuss, N. E.; Petters, M. D. The effect of hydrophobic glassy organic material on the cloud condensation nuclei activity of particles with different morphologies. *Atmos. Chem. Phys.* **2019**, *19*, 3325−3339.

(17) Zhang, Y.; Chen, Y.; Lambe, A. T.; Olson, N. E.; Lei, Z.; Craig, R. L.; Zhang, Z.; Gold, A.; Onasch, T. B.; Jayne, J. T.; Worsnop, D. R.; Gaston, C. J.; Thornton, J. A.; Vizuete, W.; Ault, A. P.; Surratt, J. D. Effect of the Aerosol-Phase State on Secondary Organic Aerosol Formation from the Reactive Uptake of Isoprene-Derived Epoxydiols (IEPDX). *Environ. Sci. Technol. Lett.* **2018**, *5*, 167−174.

(18) Shiraiwa, M.; Li, Y.; Tsimpidi, A. P.; Karydis, V. A.; Berkemeier, T.; Pandis, S. N.; Lelieveld, J.; Koop, T.; Pöschl, U. Global distribution of particle phase state in atmospheric secondary organic aerosols. *Nat. Commun.* **2017**, *8*, 15002.

(19) Berkemeier, T.; Steimer, S. S.; Krieger, U. K.; Peter, T.; Pöschl, U.; Ammann, M.; Shiraiwa, M. Ozone uptake on glassy, semi-solid and liquid organic matter and the role of reactive oxygen intermediates in atmospheric aerosol chemistry. *Phys. Chem. Chem. Phys.* **2016**, *18*, 12662−12674.

(20) Hodas, N.; Zuend, A.; Mui, W.; Flagan, R. C.; Seinfeld, J. H. Influence of particle-phase state on the hygroscopic behavior of mixed organic-inorganic aerosols. *Atmos. Chem. Phys.* **2015**, *15*, 5027−5045.

(21) Berkemeier, T.; Shiraiwa, M.; Pöschl, U.; Koop, T. Competition between water uptake and ice nucleation by glassy organic aerosol particles. *Atmos. Chem. Phys.* **2014**, *14*, 12513−12531.

(22) Ray, K. K.; Lee, H. D.; Gutierrez, M. A., Jr.; Chang, F. J.; Tivanski, A. V. Correlating 3D Morphology, Phase State and Viscoelastic Properties of Individual Substrate-Deposited Particles. *Anal. Chem.* **2019**, 7621.

(23) Zeng, C.; Liu, C.; Li, J.; Zhu, B.; Yin, Y.; Wang, Y. Optical Properties and Radiative Forcing of Aged BC due to Hygroscopic Growth: Effects of the Aggregate Structure. *J. Geophys. Res.-Atmos.* **2019**, *124*, 4620−4633.

(24) Bondy, A. L.; Bonanno, D.; Moffet, R. C.; Wang, B.; Laskin, A.; Ault, A. P. The diverse chemical mixing state of aerosol particles in the southeastern United States. *Atmos. Chem. Phys.* **2018**, *18*, 12595−12612.

(25) Wang, X.; Deane, G. B.; Moore, K. A.; Ryder, O. S.; Stokes, M. D.; Beall, C. M.; Collins, D. B.; Santander, M. V.; Burrows, S. M.; Sultana, C. M.; Prather, K. A. The role of jet and film drops in controlling the mixing state of submicron sea spray aerosol particles. *Proc. Natl. Acad. Sci. U. S. A.* **2017**, *114*, 6978−6983.

(26) Schill, S. R.; Collins, D. B.; Lee, C.; Morris, H. S.; Novak, G. A.; Prather, K. A.; Quinn, P. K.; Sultana, C. M.; Tivanski, A. V.; Zimmermann, K.; Cappa, C. D.; Bertram, T. H. The Impact of Aerosol Particle Mixing State on the Hygroscopicity of Sea Spray Aerosol. *ACS Central Sci.* **2015**, *1*, 132−141.

(27) Collins, D. B.; Ault, A. P.; Moffet, R. C.; Ruppel, M. J.; Cuadra-Rodriguez, L. A.; Guasco, T. L.; Corrigan, C. E.; Pedler, B. E.; Azam, F.; Aluwihare, L. I.; Bertram, T. H.; Roberts, G. C.; Grassian, V. H.; Prather, K. A. Impact of marine biogeochemistry on the chemical mixing state and cloud forming ability of nascent sea spray aerosol. *J. Geophys. Res.-Atmos.* **2013**, *118*, 8553−8565.

(28) Lee, H. D.; Kaluarachchi, C. P.; Hasenecz, E. S.; Zhu, J. Z.; Popa, E.; Stone, E. A.; Tivanski, A. V. Effect of dry or wet substrate deposition on the organic volume fraction of core−shell aerosol particles. *Atmos. Meas. Tech.* **2019**, *12*, 2033−2042.

(29) Riemer, N.; Ault, A. P.; West, M.; Craig, R. L.; Curtis, J. H. Aerosol Mixing State: Measurements, Modeling, and Impacts. *Rev. Geophys.* **2019**, *57*, 187−249.

(30) Lee, H. D.; Morris, H. S.; Laskina, O.; Sultana, C. M.; Lee, C.; Jayarathne, T.; Cox, J. L.; Wang, X.; Hasenecz, E. S.; DeMott, P. J.; Bertram, T. H.; Cappa, C. D.; Stone, E. A.; Prather, K. A.; Grassian, V. H.; Tivanski, A. V. Organic Enrichment, Physical Phase State, and Surface Tension Depression of Nascent Core−Shell Sea Spray Aerosols during Two Phytoplankton Blooms. *ACS Earth Space Chem.* **2020**, 650.

(31) Li, W.; Shao, L.; Zhang, D.; Ro, C.-U.; Hu, M.; Bi, X.; Geng, H.; Matsuki, A.; Niu, H.; Chen, J. A review of single aerosol particle studies in the atmosphere of East Asia: morphology, mixing state, source, and heterogeneous reactions. *J. Clean Prod.* **2016**, *112*, 1330−1349.

(32) Ault, A. P.; Moffet, R. C.; Baltrusaitis, J.; Collins, D. B.; Ruppel, M. J.; Cuadra-Rodriguez, L. A.; Zhao, D.; Guasco, T. L.; Ebben, C. J.; Geiger, F. M.; Bertram, T. H.; Prather, K. A.; Grassian, V. H. Size-Dependent Changes in Sea Spray Aerosol Composition and Properties with Different Seawater Conditions. *Environ. Sci. Technol.* **2013**, *47*, 5603−5612.

(33) Pham, D. Q.; O'Brien, R.; Fraund, M.; Bonanno, D.; Laskina, O.; Beall, C.; Moore, K. A.; Forestieri, S.; Wang, X.; Lee, C.; Sultana, C.; Grassian, V.; Cappa, C. D.; Prather, K. A.; Moffet, R. C. Biological Impacts on Carbon Speciation and Morphology of Sea Spray Aerosol. *ACS Earth Space Chem.* **2017**, *1*, 551−561.

(34) Wang, X.; Sultana, C. M.; Trueblood, J.; Hill, T. C. J.; Malfatti, F.; Lee, C.; Laskina, O.; Moore, K. A.; Beall, C. M.; McCluskey, C. S.; Cornwell, G. C.; Zhou, Y.; Cox, J. L.; Pendergraft, M. A.; Santander, M. V.; Bertram, T. H.; Cappa, C. D.; Azam, F.; DeMott, P. J.; Grassian, V. H.; Prather, K. A. Microbial Control of Sea Spray Aerosol Composition: A Tale of Two Blooms. *ACS Cent. Sci.* **2015**, *1*, 124−131.

(35) Prather, K. A.; Bertram, T. H.; Grassian, V. H.; Deane, G. B.; Stokes, M. D.; DeMott, P. J.; Aluwihare, L. I.; Palenik, B. P.; Azam, F.; Seinfeld, J. H.; Moffet, R. C.; Molina, M. J.; Cappa, C. D.; Geiger, F. M.; Roberts, G. C.; Russell, L. M.; Ault, A. P.; Baltrusaitis, J.; Collins,

https://dx.doi.org/10.1021/acsearthspacechem.0c00153
ACS Earth Space Chem. 2020, 4, 1604−1611

D. B.; Corrigan, C. E.; Cuadra-Rodriguez, L. A.; Ebben, C. J.; Forestieri, S. D.; Guasco, T. L.; Hersey, S. P.; Kim, M. J.; Lambert, W. F.; Modini, R. L.; Mui, W.; Pedler, B. E.; Ruppel, M. J.; Ryder, O. S.; Schoepp, N. G.; Sullivan, R. C.; Zhao, D. Bringing the ocean into the laboratory to probe the chemical complexity of sea spray aerosol. *Proc. Natl. Acad. Sci. U. S. A.* **2013**, *110*, 7550−7555.

(36) Schauer, J. J.; Mader, B. T.; Deminter, J. T.; Heidemann, G.; Bae, M. S.; Seinfeld, J. H.; Flagan, R. C.; Cary, R. A.; Smith, D.; Huebert, B. J.; Bertram, T.; Howell, S.; Kline, J. T.; Quinn, P.; Bates, T.; Turpin, B.; Lim, H. J.; Yu, J. Z.; Yang, H.; Keywood, M. D. ACE-Asia intercomparison of a thermal-optical method for the determination of particle-phase organic and elemental carbon. *Environ. Sci. Technol.* **2003**, *37*, 993−1001.

(37) Jayarathne, T.; Sultana, C. M.; Lee, C.; Malfatti, F.; Cox, J. L.; Pendergraft, M. A.; Moore, K. A.; Azam, F.; Tivanski, A. V.; Cappa, C. D.; Bertram, T. H.; Grassian, V. H.; Prather, K. A.; Stone, E. A. Enrichment of Saccharides and Divalent Cations in Sea Spray Aerosol During Two Phytoplankton Blooms. *Environ. Sci. Technol.* **2016**, *50*, 11511−11520.

(38) Jayarathne, T.; Stockwell, C. E.; Yokelson, R. J.; Nakao, S.; Stone, E. A. Emissions of Fine Particle Fluoride from Biomass Burning. *Environ. Sci. Technol.* **2014**, *48*, 12636−12644.

(39) Holland, H. D., *The chemistry of the atmosphere and oceans*; Wiley-Interscience, 1978 p xiv, 351 pages.

(40) Shiraiwa, M.; Ammann, M.; Koop, T.; Pöschl, U. Gas uptake and chemical aging of semisolid organic aerosol particles. *Proc. Natl. Acad. Sci. U. S. A.* **2011**, *108*, 11003−11008.

(41) Or, V. W.; Estillore, A. D.; Tivanski, A. V.; Grassian, V. H. Lab on a tip: atomic force microscopy - photothermal infrared spectroscopy of atmospherically relevant organic/inorganic aerosol particles in the nanometer to micrometer size range. *Analyst* **2018**, 2765.

(42) Ghorai, S.; Laskin, A.; Tivanski, A. V. Spectroscopic Evidence of Keto−Enol Tautomerism in Deliquesced Malonic Acid Particles. *J. Phys. Chem. A* **2011**, *115*, 4373−4380.

(43) Shao, X.; Zhang, Y.; Pang, S.-F.; Zhang, Y.-H. Vacuum FTIR observation on hygroscopic properties and phase transition of malonic acid aerosols. *Chem. Phys.* **2017**, *483-484*, 7−11.

(44) Ganguly, S.; Fernandes, J. R.; Desiraju, G. R.; Rao, C. N. R. Phase transition in malonic acid: An infrared study. *Chem. Phys. Lett.* **1980**, *69*, 227−229.

(45) Boyd, I. W.; Wilson, J. I. B. A study of thin silicon dioxide films using infrared absorption techniques. *J. Appl. Phys.* **1982**, *53*, 4166−4172.

(46) Weis, D. D.; Ewing, G. E. Infrared spectroscopic signatures of (NH4)2SO4 aerosols. *J. Geophys. Res. Atmos.* **1996**, *101*, 18709−18720.

(47) Lahiri, B.; Holland, G.; Centrone, A. Chemical Imaging Beyond the Diffraction Limit: Experimental Validation of the PTIR Technique. *Small* **2013**, *9*, 439−445.

(48) Ault, A. P.; Axson, J. L. Atmospheric Aerosol Chemistry: Spectroscopic and Microscopic Advances. *Anal. Chem.* **2017**, *89*, 430−452.

https://dx.doi.org/10.1021/acsearthspacechem.0c00153
ACS Earth Space Chem. 2020, 4, 1604−1611